Yang, Linlin; He, Ren; Wang, Xiang; [et al.]. «Self-supported NiO/CuO electrodes to boost urea oxidation in direct urea fuel cells». Nano Energy, Vol. 115 (October 2023), art. 108714. DOI 10.1016/j.nanoen.2023.108714

Self-supported NiO/CuO electrodes to boost urea oxidation in direct urea fuel cells

Linlin Yang[a,b], Ren He[a,b], Xiang Wang[a], Tingting Yang[c], Ting Zhang[d], Yong Zuo[a,e], Xuan Lu[a], Zhifu Liang [a,d], Junshan Li[f], Jordi Arbiol[d,g], Paulina R. Martínez-Alanis[a,b]*, Xueqiang Qi[a,h]*, and Andreu Cabot[a,g]*

a Catalonia Energy Research Institute – IREC, Sant Adrià de Besòs, 08930, Barcelona, Catalonia, Spain

b Universitat de Barcelona, 08028, Barcelona, Catalonia, Spain

c College of Chemistry and Chemical Engineering, Chongqing University of Technology, Chongqing, 400054, China

d Catalan Institute of Nanoscience and Nanotechnology (ICN2), CSIC, BIST, Campus UAB, Bellaterra, 08193, Catalonia, Spain

e Nanochemistry Department, Istituto Italiano di Tecnologia, Via Morego 30, 16163, Genova, Italy

f Institute of Advanced Study, Chengdu University, Chengdu, 610106, China

g ICREA, Pg. Lluis Companys, 08010, Barcelona, Catalonia, Spain

h College of Chemistry and Chemical Engineering, Chongqing University, Chongqing, 400044, China

* Corresponding authors

E-mail addresses: pmartinez@irec.cat (Paulina R. Martínez-Alanis), xqqi@cqut.edu.cn (XueQiang Qi), acabot@irec.cat (Andreu Cabot)

ABSTRACT

Direct urea fuel cells (DUFCs) can be used to treat residual wastewater while generating electricity. Herein, self-supported electrodes consisting of NiO nanosheets vertically grown on CuO nanowires are synthesized to realize the urea oxidation reaction (UOR). Such electrodes show excellent UOR performance requiring 1.39 V vs. RHE to achieve 100 mA/cm^2. Besides, DUFCs provide open circuit voltages and power densities up to 0.88 V and 11.35 mW/cm^2. Electrochemical characterization and Raman spectroscopy prove the formation of NiOOH to enable the UOR. Mott-Shotky analysis and UV photoelectron spectroscopy show the NiO/CuO p-p heterostructure to facilitate the charge transfer from CuO nanowires to NiO nanosheets. Besides, at a local level, density functional theory calculations show that the presence of CuO modulates the electronic states of Ni at the very NiOOH/CuO interface, which results in stretched Ni-O bonds and a uniquely elongated N-H bond of urea that favors its oxidation.

KEYWORDS: Urea, urea oxidation reaction, electrocatalysis, nickel oxyhydroxide, copper, direct urea fuel cell.

1. Introduction

Huge amounts of urea ($CO[NH_2]_2$) are industrially produced as fertilizers and naturally generated in livestock farming. Such massive production of urea releases large amounts of wastewater polluted with ammonium into the environment, which is a major concern for environmentally sustainable development. Not only do aquatic ecosystems close to intensive farms suffer from major urea-derived pollution, but ammonia released by urea combines with other pollutants to form particulate matter that affects human health, can release nitrous oxide, which is a powerful greenhouse gas, and raise acidity levels.[1] Thus, direct urea fuel cells (DUFCs), generating electric power from the electrooxidation of urea have great potential as a cost-effective technology to simultaneously treat urea-containing wastewater and produce electricity.[2,3] DUFCs release only gaseous products, not generating new waste, and they are characterized by a relatively high theoretically open circuit voltage (OCV) of 1.147 V, similar to that of hydrogen fuel cells.[4,5] However, the relatively low OCVs and peak power densities realized so far have hindered their commercialization. Therefore, improving the OCVs and peak power densities of DUFCs using low-cost and abundant catalysts is required to ensure practical significance.

The cell activity toward the urea oxidation reaction (UOR) determines the overall performance of the DUFC.[6] UOR can be reached by a six-electron transfer process.[7]

$$CO(NH_2)_2 + 6OH^- \rightarrow N_2 + 5H_2O + CO_2 + 6e^- \quad (1)$$

Despite involving six electrons, the UOR has been also proposed as a lower thermodynamic potential (0.37 V) alternative to the oxygen evolution reaction (OER, 1.23 V) for the electrochemical generation of hydrogen.[8-10] While noble metals such as Pt, Ir, and Ru are the benchmark UOR catalysts,[11] the development of high activity and stable UOR catalysts based on abundant elements is fundamental to achieving a cost-effective DUFC technology. Recently, Cu- and Ni-based electrocatalysts have received extensive attention for electro-oxidation reactions, including UOR,[12,13] OER,[14,15] and the oxidation of ethanol,[16,17] methanol,[18,19] and glucose.[20,21] A possible UOR electrocatalytic process on Cu- and Ni-based catalysts have been reported to take place at CuOOH or NiOOH surface sites through the following intermediates (2-9).[5,22-25]

$$CO(NH_2)_2 + M \rightarrow [M.CO(NH_2)_2]_{ads} \tag{2}$$

$$[M.CO(NH_2)_2]_{ads} + OH^- \rightarrow [M.CO(NH{\cdot}NH_2)]_{ads} + H_2O + e^- \tag{3}$$

$$[M.CO(NH_2NH)]_{ads} + OH^- \rightarrow [M.CO(NH{\cdot}NH)]_{ads} + H_2O + e^- \tag{4}$$

$$[M.CO(NH_2N)]_{ads} + OH^- \rightarrow [M.CO(NH{\cdot}N)]_{ads} + H_2O + e^- \tag{5}$$

$$[M.CO(NHN)]_{ads} + OH^- \rightarrow [M.CO(N_2)]_{ads} + H_2O + e^- \tag{6}$$

$$[M.CO(N_2)]_{ads} + OH^- \rightarrow [M.CO{\cdot}OH]_{ads} + N_2 + e^- \tag{7}$$

$$[M.COOH]_{ads} + OH^- \rightarrow [M.COO]_{ads} + H_2O + e^- \tag{8}$$

$$[M.COO]_{ads} + 2OH^- \rightarrow CO_3^{2-} + M \tag{9}$$

Frequently, the strong bond created between Ni^{3+} and *COO hinders its desorption and limits the performance of UOR, but other rate-limiting steps have also been reported.[26,27]

In terms of composition, beyond single-phase catalysts, heterostructured materials provide additional degrees of freedom to optimize electrochemical performance. The construction of heterostructures is for instance an effective strategy to modulate the adsorption properties of a material both by tuning the electronic structure at the very interface between the two materials and by redistributing charge carriers and generating an internal built-in electric field able to boost charge injection at a larger scale (1-100 nm).[28-30]

In terms of material architecture, 2D nanosheet (NS) assemblies with high specific surface area and hierarchically porous structure are a particularly appealing class of materials to simultaneously maximize active site exposure and mass transport. Besides, compared with the production of electrodes through the deposition of a catalyst ink on a current collector, the direct growth of the catalyst from high surface area electrodes such as carbon cloth, carbon paper, nickel foam, copper foam, or stainless mesh, provides several advantages to boost the electrocatalytic performance, including i) no glue/binder such as Nafion is needed to adhere the catalysts to the electrode, thus maximizing the number of accessible surface sites, charge transfer and diffusivity of relevant species; ii) the lack of agglomeration generally results in larger specific surface areas; iii) the improved dispersion of the catalysts prevents blocking the diffusion of reactants and products; iv) the direct growth of the catalyst with a potential crystallographic continuity further promotes electron transfer and durability.

In this work, a p-p heterojunction catalyst is directly grown from the surface of a copper mesh (CuM) current collector. More specifically, 2D NiO NSs are grown on the surface of 1D CuO nanowires (NWs) that are in turn directly grown on the surface of CuM. The hierarchically architectured electrode obtained (denoted as NiO/CuO@CuM) is evaluated for the electrochemical UOR. The active sites on the catalyst surface, the role of the built-in electric field and the potential role of the interface between the two materials are thoroughly investigated both experimentally and using density functional theory (DFT) calculations. Finally, DUFCs based on the optimized NiO/CuO@CuM anode are assembled and tested.

2. Experimental

2.1. Materials and reagents

Nickel nitrate hexahydrate ($Ni(NO_3)_2 \cdot 6H_2O$, 99 %, fisher), urea ($CO(NH_2)_2$, 99.3 %, sigma), ammonium persulfate (APS, $(NH4)_2S_2O_8$, 98 %, sigma), sodium hydroxide (NaOH, 98 %, fisher), hydrochloric acid, 37 %, ethanol, 96 %, and acetone, 99.6 % were used as received without further purification. A CuM with a wire diameter of about 200 μm and a pore size of 400 μm was purchased from Kunshan GuangJiaYuan New Materials Co. Ltd. Deionized water (DI water, 18.6 MΩ cm) obtained using a purification system (Purelab flex, ELGA) was used for all experiments.

2.2. Synthesis of Catalysts

Synthesis of $Cu(OH)_2$@CuM: $Cu(OH)_2$ NWs were grown on the surface of CuM following our previously reported procedure. Briefly, a piece of CuM (2 cm×1 cm) was thoroughly cleaned using ethanol/acetone and HCl (1 mol/L) for 30 min and then rinsed with plenty of DI water. The cleaned CuM was then immersed in a solution of NaOH (40 mmol), APS (2 mmol), and DI water (20 mL) at room temperature for 30 min. During this time, the color of CuM changed from tan to blue. The obtained $Cu(OH)_2$@CuM was washed carefully using DI water and then dried under nitrogen flow.

Synthesis of CuO@CuM: CuO@CuM was obtained by annealing $Cu(OH)_2$@CuM under a synthetic air atmosphere for 2 h at 350 °C with a temperature ramp of 5 °C/min.

Synthesis of $Ni(OH)_2/Cu(OH)_2$@CuM: The $Cu(OH)_2$@CuM was used as a template for preparing $Ni(OH)_2/Cu(OH)_2$@CuM and NiO/CuO@CuM. Briefly, 0.075 M $Ni(NO_3)_2$, 1.13 M urea, and 20 mL DI water were added into a 50 mL flask with a magnetic stirrer until obtaining a clear solution. Then the solution was heated to 80 °C with a temperature ramp of 5 °C/min. When the temperature was stable, a piece of $Cu(OH)_2$@CuM was introduced into the solution and left to react for 1 h. Afterward, the product was washed with DI water and dried with N_2.

Synthesis of NiO/CuO@CuM: NiO/CuO@CuM was obtained by annealing the $Ni(OH)_2/Cu(OH)_2$@CuM sample under a synthetic air atmosphere for 2 h at 350 °C with a temperature ramp of 5 °C/min.

2.3.Characterization

Catalyst physicochemical characterization: Morphological and elemental analyses were carried out using a scanning electron microscope (SEM) from Carl Zeiss combined with an Oxford energy dispersive X-ray spectrometer (EDS). The crystal structure of the samples was determined by X-ray diffraction (XRD) using a Bruker D8 Advance diffractometer with Ni-filtered Cu-Kα radiation (λ = 0.15406 Å) operating at 40 mA and 40 kV. XRD characterization was carried out on the powder materials collected from the sonication of the electrodes, i.e. without the CuM substrate to eliminate its influence. X-ray photoelectron spectroscopy (XPS) and ultraviolet photoelectron spectroscopy (UPS) were carried out on a SPECS system equipped with an Al anode XR50 source operating at 150 mW and a Phoibos 150 MCD-9 detector. High-resolution transmission electron microscopy (HRTEM) images and scanning transmission electron microscopy (STEM) studies were conducted on an FEI Tecnai F20 field emission gun microscope operated at 200 kV with a point-to-point resolution of 0.19 nm, which was also equipped with high-angle annular dark-field (HAADF) and Gatan Quantum electron energy loss spectroscopy (EELS) detectors.

Electrocatalytic activity evaluation: All electrochemical characterizations were conducted on a CHI760E electrochemical workstation (Shanghai, Chenhua) using a standard three-electrode configuration in 1.0 M KOH with different concentrations of urea. The self-supported catalyst on CuM was used as the working electrode with an effective area of 1×0.8 cm^2, a platinum wire was used as the counter electrode, and Hg/HgO was used as the reference electrode. All measured potentials ($E_{Hg/Hgo}$) were converted to the reversible hydrogen electrode (RHE) potential through the Nernst equation ($E_{RHE} = E_{Hg/Hgo} + 0.0591 \times pH + 0.098$). All the measurements were recorded at room temperature. Linear scanning voltammetry (LSV) was carried out at a scan rate of 5 mV/s with 90 % IR_s correction. Tafel slopes were calculated from the corresponding LSV curves according to the equation ($E = a + b \log j$), where j is the current density, and b is the Tafel slope.

Double layer capacitances (C_{dl}) were obtained from cyclic voltammetry (CV) curves at different scan rates (v) from 10-100 mV/s through the equation ($i = vC_{dl}$), where i is the measured current.

The electrochemical active surface area (ECSA) of electrodes was calculated according to the equation ($ECSA = C_{dl}/C_s$), where C_s=0.04 mF/cm^2.[31] Electrochemical impedance spectroscopy (EIS) spectra were obtained at 1.36 V vs. RHE in the frequency range from 100 kHz to 0.01 Hz. Stability was analyzed by chronopotentiometry at a current density of 10 mA/cm^2. Two types of DUFCs were assembled. One of them was based on an anolyte containing 1.0 M KOH and 0.5 M urea, a 0.1 M KOH catholyte, and a Fumasep FAA-3-PK-130 as the anion exchange membrane. The other one was based on an anolyte containing 1.0 M KOH and 0.5 M urea, a catholyte containing 2 M H_2O_2 and 2 M H_2SO_4, and a Nafion 117 as the proton exchange membrane. The volume of the cathode and anode chambers was 30 mL.

2.4. Electrochemical calculations

The flat band potential (E_{fb}) and charge carrier concentration (N_D) were determined through the fitting of the interphase capacitance (C) dependence on the applied voltage through the Mott–Schottky equation (10):

$$\frac{1}{C^2} = \frac{2}{\varepsilon\varepsilon_0 A^2 e N_D}\left(V - E_{fb} - \frac{K_B T}{e}\right) \qquad (10)$$

where A is the interphase area, ε is the dielectric constant of the semiconductor, ε_0 is the permittivity of free space, K_B is Boltzmann's constant, T is the absolute temperature, and e is the electronic charge.

The Fermi level (E_{Fermi}) is determined through equation (11):[32-34]

$$E_{Fermi} = hv - (E_{cutoff} - E_f) \tag{11}$$

where hv is 21.22 eV for the He I laser energy of the UPS measurements. E_{cufoff} and E_f can be directly obtained through UPS spectra, which are the cut-off and Fermi energy of the secondary electrons.

2.5. DFT calculations

Spin-polarized DFT calculations were carried out to study the energetic and electronic properties of pristine CuO, NiOOH, and the NiOOH/CuO interphase, respectively. The generalized gradient approximation (GGA) with parametrization by Perdew-Burke-Ernzerhof (PBE) was adopted for exchange-correlation potential. The interaction between the ionic core and valence electrons was treated by ultrasoft pseudopotential. A cut-off energy of a plane-wave basis was set as 300 eV, and the Monkhorst-Pack k-point sampling was generated with a 2×2×1 grid. The convergence threshold for the displacement tolerance, maximum force and maximum energy change were set to be 0.002 Å, 0.05 eV/Å and 2.0×10^{-5} eV/atom, respectively. A vacuum layer with a 15 Å thickness was used along the z-direction to eliminate the interactions between different surfaces. The adsorption energy of urea and CO_2 on CuO, NiOOH, and NiOOH/CuO was calculated according to the equation (12):

$$E_{ads} = E_{total} - (E_{slab} + E_{adsorbate}) \tag{12}$$

Where E_{ads} is the adsorption energy, E_{total} is the total energy for the adsorption state, E_{slab} is the energy of the clean surface of CuO, NiOOH, or NiOOH/CuO, and $E_{adsorbate}$ is the energy of either free urea or free CO_2 molecules.

3. Results and Discussion.

3.1. Catalyst characterization

NiO/CuO heterojunctions were grown on a CuM support via a three-step process (**Fig. 1**a). In the first step, $Cu(OH)_2$ was grown on the CuM surface by etching the copper framework in the presence of APS and NaOH. According to SEM and XRD characterization, the produced $Cu(OH)_2$ displays NW morphology and an orthorhombic $Cu(OH)_2$ phase (**Figs. 1**b and Fig. S1). In the second step, $Ni(OH)_2$ was grown on the surface of the $Cu(OH)_2$ NWs. **Figs. 1**c and S2 show the $Ni(OH)_2$ to be characterized by NS morphology and the theophrastite hexagonal crystal phase. In the third step, the $Ni(OH)_2/Cu(OH)_2$@CuM was annealed at 350 ºC under synthetic air to produce NiO/CuO@CuM. As shown in **Figs. 1**d, NiO/CuO@CuM maintains the NW and NS morphologies of the Cu- and Ni-based materials respectively, and the CuO NWs are fully covered by NiO NSs. As observed by XRD analysis, the composite contains both tenorite monoclinic CuO and bunsenite cubic NiO phases (Figure S3).

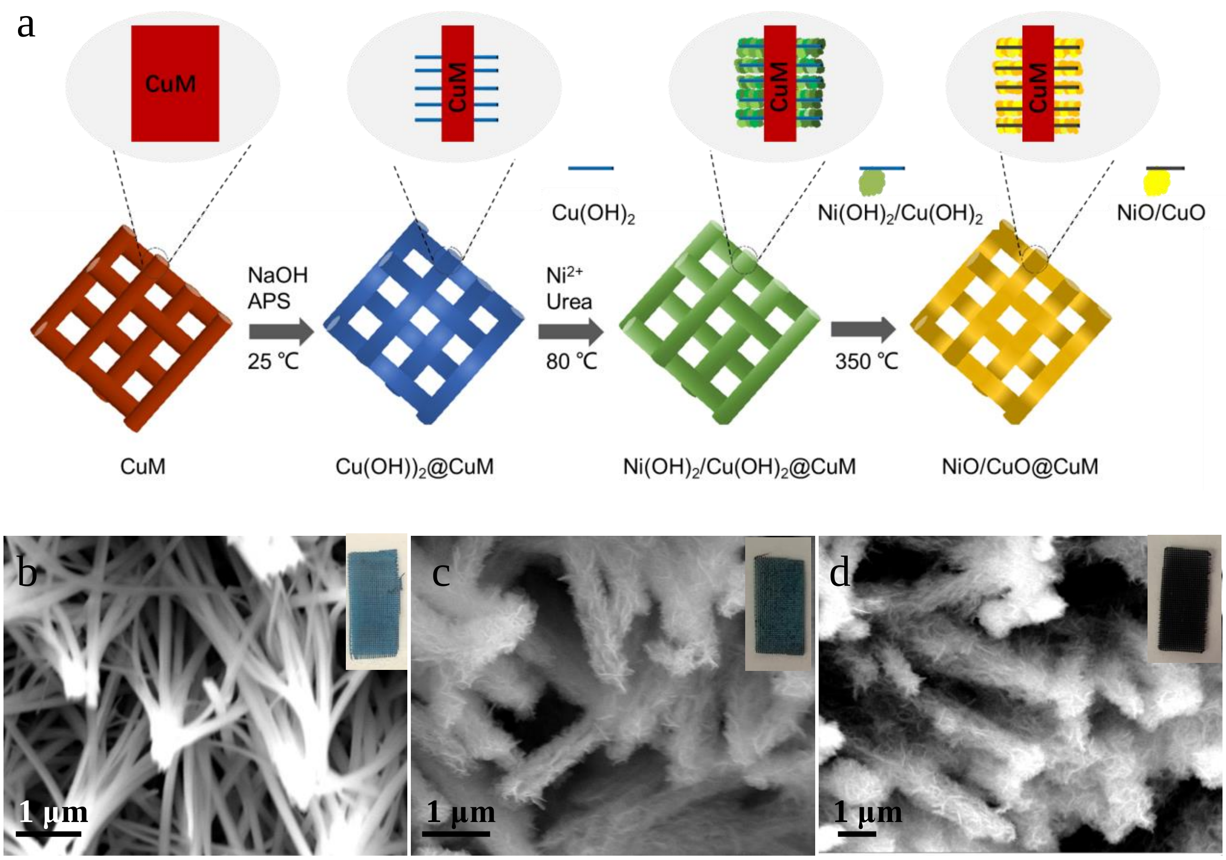

Fig. 1. (a) Scheme of the NiO/CuO@CuM electrode preparation process. (b-d) SEM images of (b) Cu(OH)$_2$@CuM, (c) Ni(OH)$_2$/Cu(OH)$_2$@CuM, (d) NiO/CuO@CuM. Insets show optical images of the self-supported electrode.

Fig. 2a shows a TEM image of the NiO/CuO heterostructure displaying a large density of NiO NSs around the CuO NWs. HRTEM micrographs and the indexed fast Fourier transform (FFT) reveal the presence of both the bunsenite cubic phase of NiO and the tenorite monoclinic phase of CuO (**Fig. 2**b-e). The CuO NWs obtained from Cu(OH)$_2$ show a highly polycrystalline nature and no preferential orientation between the two oxide phases, NiO and CuO, is observed. Additional HRTEM images of tenorite monoclinic CuO and bunsenite cubic NiO are shown in Figs. S4 and S5. **Fig. 2**f displays a HAADF STEM micrograph and its corresponding EELS elemental maps of the NiO/CuO heterostructure. EELS maps show oxygen to be uniformly distributed throughout all the nanostructures, while Ni is mostly localized in the NSs, and Cu in the NWs.

As a reference material, CuO@CuM was obtained from the annealing of $Cu(OH)_2$@CuM in the same conditions used to produce NiO/CuO@CuM. As displayed in Figs. S6a and b, the annealed material inherited the NW-based morphology of $Cu(OH)_2$@CuM but presented the tenorite monoclinic CuO crystal phase. EELS revealed CuO@CuM to contain a homogeneous distribution of Cu and O (Fig. S7). Additionally, we also tried to obtain the reference NiO@CuM and $Ni(OH)_2$@CuM samples, but as shown in Fig. S8, the $Ni(OH)_2$ NSs could not directly grow on the surface of the CuM without the $Cu(OH)_2$ interphase.

XPS was used to investigate the surface chemistry of CuO@CuM and NiO/CuO@CuM. Fig. S9 displays the survey XPS spectra of these two electrodes. The low peak intensity of Cu 2p in NiO/CuO@CuM demonstrates that most of the CuO surface is covered by NiO. Quantitatively, the surface atomic content probed by XPS is shown in Table S1. Only 5.04 % Cu atoms were detected on the surface of NiO/CuO@CuM, in contrast to the 24.47 % detected by EDS. **Figs. 2**g-i show the high-resolution Ni 2p, Cu 2p, and O 1s XPS spectra of the two electrodes. The high-resolution Ni 2p XPS spectrum of NiO/CuO@CuM resembles that of Ni^{2+} within NiO, with a Ni 2p doublet at 853.9 eV (Ni $2p_{3/2}$) and 871.7 eV (Ni $2p_{1/2}$) and two additional satellite peaks (**Fig. 2**g). The Cu 2p XPS spectrum in NiO/CuO@CuM displays a doublet at 933.1 eV (Cu $2p_{3/2}$) and 953.0 eV (Cu $2p_{3/2}$), and two satellite peaks, which point to the presence of Cu^{2+} in a CuO chemical environment. Compared with CuO@CuM, the Cu 2p binding energy of NiO/CuO@CuM shifts negatively by 0.8 eV, indicating a higher electron density on the surface of CuO within NiO/CuO@CuM (**Fig. 2**h). The O 1s XPS spectrum of both CuO@CuM and NiO/CuO@CuM display three contributions (**Fig. 2**i). The O 1s contribution at the lowest binding energy (529.1 eV for NiO/CuO@CuM) is assigned to lattice oxygen (O_L). The binding energy of this component is positively shifted for NiO/CuO@CuM compared with CuO@CuM due to the different oxide coordination environments. The main contribution, at 530.6 eV for NiO/CuO@CuM, comes from adsorbed oxygen-containing species including OH groups (O_{OH}). This component is frequently associated with the presence of oxygen vacancies acting as surface adsorption sites for oxygen-containing species.[35,36] NiO/CuO@CuM displays a larger contribution of the adsorbed oxygen species (56.3 %) compared with that of CuO@CuM (50.7 %), implying a higher density of surface sites. The third minor O 1s band, at 532.6 eV for NiO/CuO@CuM, is associated with adsorbed water molecules (O_{H_2O}).

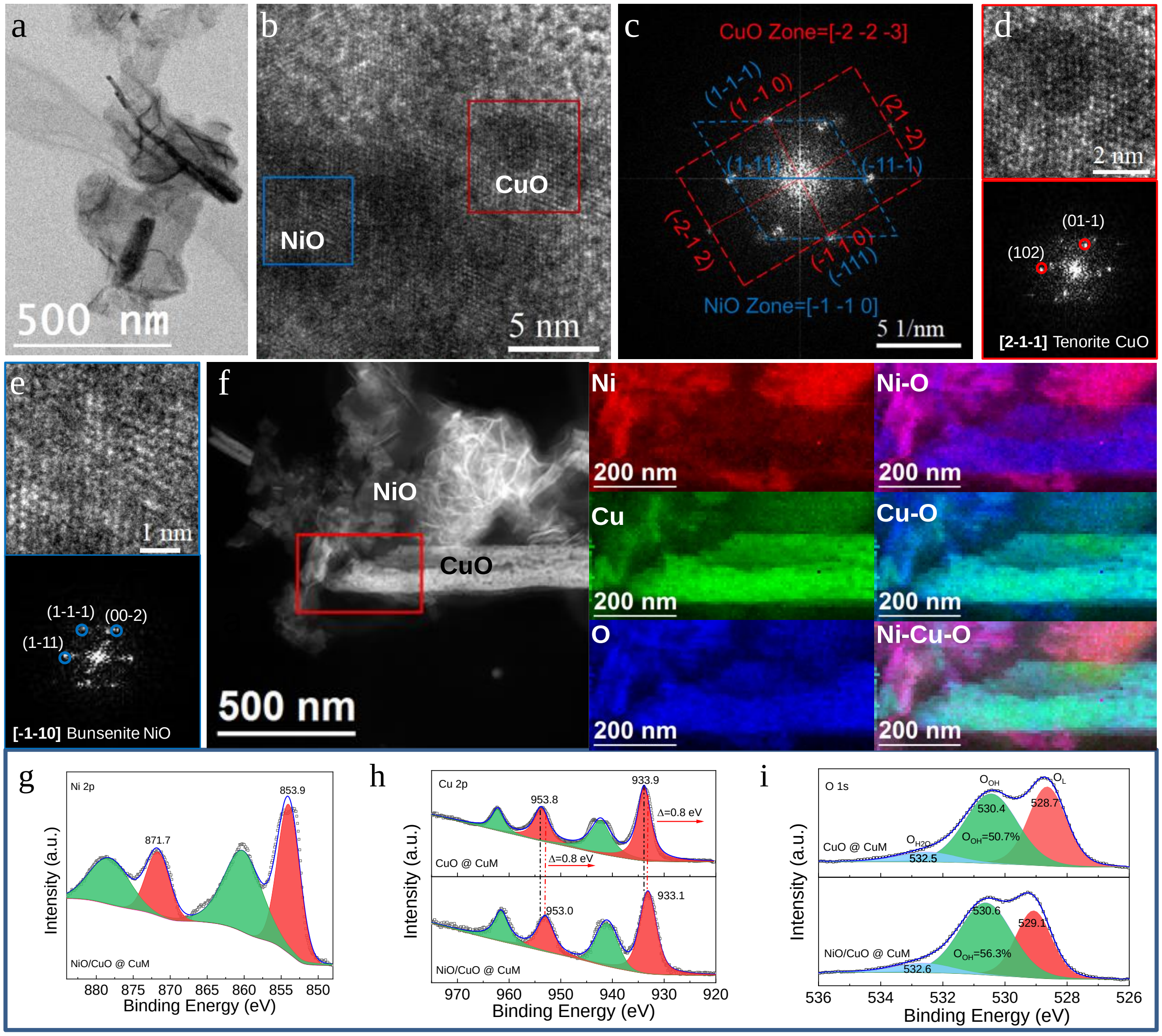

Fig. 2. (a) TEM image of NiO/CuO. (b) HRTEM images and (c) corresponding indexed FFT of a NiO/CuO heterostructure showing the overlapping NiO and CuO phases. (d-e) HRTEM images and corresponding indexed FFT of CuO (red square) and NiO (blue square) phases shown in (b). (f) HAADF STEM micrograph and EELS elemental maps of a NiO/CuO heterostructure (Ni = red, Cu = green, O = blue). (g-i) High-resolution Ni 2p (g), Cu 2p (h), and O 1s (i) XPS spectra of CuO@CuM and NiO/CuO@CuM.

3.2. Catalyst performance

The NiO/CuO@CuM electrode was first analyzed by LSV in 1.0 M KOH electrolyte with and without 0.5 M urea. As shown in **Fig. 3**a, in both electrolytes a sharp current increase is observed at about 1.35 V vs. RHE. In the 1.0 M KOH electrolyte, the small current increase is related to the oxidation of Ni^{2+} to Ni^{3+}, to form NiOOH. In the presence of 0.5 M urea, the Ni^{2+} oxidation triggers a large increase in current associated with the UOR, which points to Ni^{3+} as the UOR catalytic site. On the other hand, the OER current emerges at significantly larger voltages of about 1.6 V vs. RHE.

The UOR performance of the NiO/CuO@CuM electrode in 1.0 M KOH electrolyte with different concentrations of urea is displayed in **Fig. 3**b. The UOR activity strongly increases with the urea concentration at high current densities (Fig. S10), but the onset potential and the activity near this onset are independent of the urea concentration which further points to the oxidation of Ni^{2+} to Ni^{3+} active species as the UOR enabling step.

The electrocatalytic UOR activity of the different self-supported electrodes was characterized by LSV in 1.0 M KOH electrolyte containing 0.5 M urea. As shown in **Fig. 3**c, the NiO/CuO@CuM electrode requires 1.35 V to drive a current density of 10 mA/cm^2 and only 1.39 V to drive 100 mA/cm^2. The $Ni(OH)_2/Cu(OH)_2$@CuM electrode shows a lower activity than NiO/CuO@CuM, requiring 1.37 V to drive 10 mA/cm^2. On the other hand, CuO@CuM and $Cu(OH)_2$@CuM electrodes display much lower UOR activities, requiring 1.44 V and 1.47 V to reach 10 mA/cm^2, which again points to Ni^{3+} as the main UOR active site in the NiO/CuO@CuM.

As shown in **Fig. 3**d, the NiO/CuO@CuM electrode exhibits a Tafel slope of 32.2 mV/dec, much lower than that of $Ni(OH)_2/Cu(OH)_2$@CuM (63.2 mV/dec), CuO@CuM (98.7 mV/dec) and $Cu(OH)_2$@CuM (100.1 mV/dec) electrodes, which demonstrates that the NiO/CuO@CuM electrode has the fastest UOR reaction kinetics. To further study the active surface area, the C_{dl} of different self-supported electrodes was calculated from CV curves with different scan rates (**Fig.**

3e and Fig. S11). As expected, the NiO/CuO@CuM electrode exhibits the largest C_{dl} value (8.08 mF/cm^2) among the tested electrodes, which is 1.1 times that of $Ni(OH)_2/Cu(OH)_2$@CuM (7.41 mF/cm^2), and 3.7 times that of CuO@CuM (2.16 mF/cm^2) and $Cu(OH)_2$@CuM (2.17 mF/cm^2) electrodes. Furthermore, the ECSA values of the different electrodes were also calculated (Fig. S12). NiO/CuO@CuM has the largest ECSA at 141.40 cm^2, larger than that of $Ni(OH)_2/Cu(OH)_2$@CuM (129.68 cm^2), CuO@CuM (37.80 cm^2) and $Cu(OH)_2$@CuM (37.98 cm^2) . The LSV curves normalized to ECSA are shown in **Fig. 3**f.

The Nyquist plots from EIS data are shown in **Fig. 3**g. The NiO/CuO@CuM electrode provides the lowest charge transfer resistance (R_{ct}) among all the self-supported electrodes, which is related to its fastest UOR kinetics. Furthermore, the NiO/CuO@CuM electrode displays the largest electrical conductivity, 4.30×10^6 S/m, much higher than that of $Ni(OH)_2/Cu(OH)_2$@CuM (1.76×10^6 S/m), CuO@CuM (5.1×10^5 S/m), and $Cu(OH)_2$@CuM (6×10^4 S/m) electrodes (**Fig. 3**h). Overall, compared with the reference electrodes and previous reports, the NiO/CuO@CuM electrode demonstrates a high UOR performance attributed to its fast reaction kinetics, large active surface area, low R_{ct}, and high electrical conductivity (**Fig. 3**i and Table S2).

The stability of NiO/CuO@CuM electrode was investigated by chronopotentiometry (i–t). As displayed in **Fig. 3**j, the NiO/CuO@CuM electrode shows excellent long-term stability with a minor current density decrease (5 %) at the potential of 1.35 V vs. RHE after 36 h measurement. Besides, after long-term chronoamperometry measurement, only a 0.05 V increment of potential is required for NiO/CuO@CuM electrode to drive the current density of 10 mA/cm^2 (Fig. S13). SEM and XRD characterization of the NiO/CuO@CuM electrode after the stability test shows no obvious morphology deterioration nor crystalline damage on the Ni-based NSs and the CuO NWs, indicating a high morphological and structural stability (Figs. S14 and S15). The Ni-based NSs still encapsulated the CuO NWs. It is worth noting that the electrode maintains the monoclinic CuO phase but no obvious XRD peaks can be indexed to the Ni-based phase, consistently with Ni instead of Cu being the active UOR site and participating in the UOR reaction. As shown from the XPS spectra (Fig. S16), after the stability test, the Cu 2p doublet is located at 933.5 eV and 953.3 eV, thus has just a small positive shift of ca. 0.3 eV compared with the original NiO/CuO@CuM electrode, confirming its stability during the UOR. In contrast, the binding energies of Ni 2p peaks of the NiO/CuO@CuM electrode after the stability test are positively shifted to 855.4 eV and 873.1 eV, i.e. about 1.4 eV with respect to the initial material. This notable shift is associated with the oxidation of the Ni atoms to form the metal oxyhydroxide phase during the UOR.[37]

Raman spectra of the NiO/CuO@CuM electrode were also measured before and after the UOR stability test. Before the UOR test, as shown in Fig. S17, an obvious Raman peak at 518 cm^{-1} confirms the Ni-O bond for NiO.[38] No peaks attributed to CuO are detected, consistent with the CuO being mostly covered by NiO. After the UOR stability test, the Raman peak observed at 460 cm^{-1} is associated with the Ni-O(H) stretching vibration for $Ni(OH)_2$,[39] and the peak at 591 cm^{-1} is assigned to the A_{1g} Ni-O stretching vibration for NiOOH.[40] Besides, a Raman mode at 345 cm^{-1} can be assigned to the Cu-O bond of CuO.[41] The Cu signal was detected due to the loose $NiO/Ni(OH)_2/NiOOH$ NS structure after the stability test. These results confirm that during UOR, NiO transforms to $Ni(OH)_2$ and NiOOH, while CuO remains constant without generating CuOOH, which is consistent with the XPS analysis results. Overall, combining SEM, XRD, XPS, Raman and electrochemical analyses, we can conclude that upon UOR, NiO is oxidized to NiOOH which is the main active site in the NiO/CuO@CuM electrode.

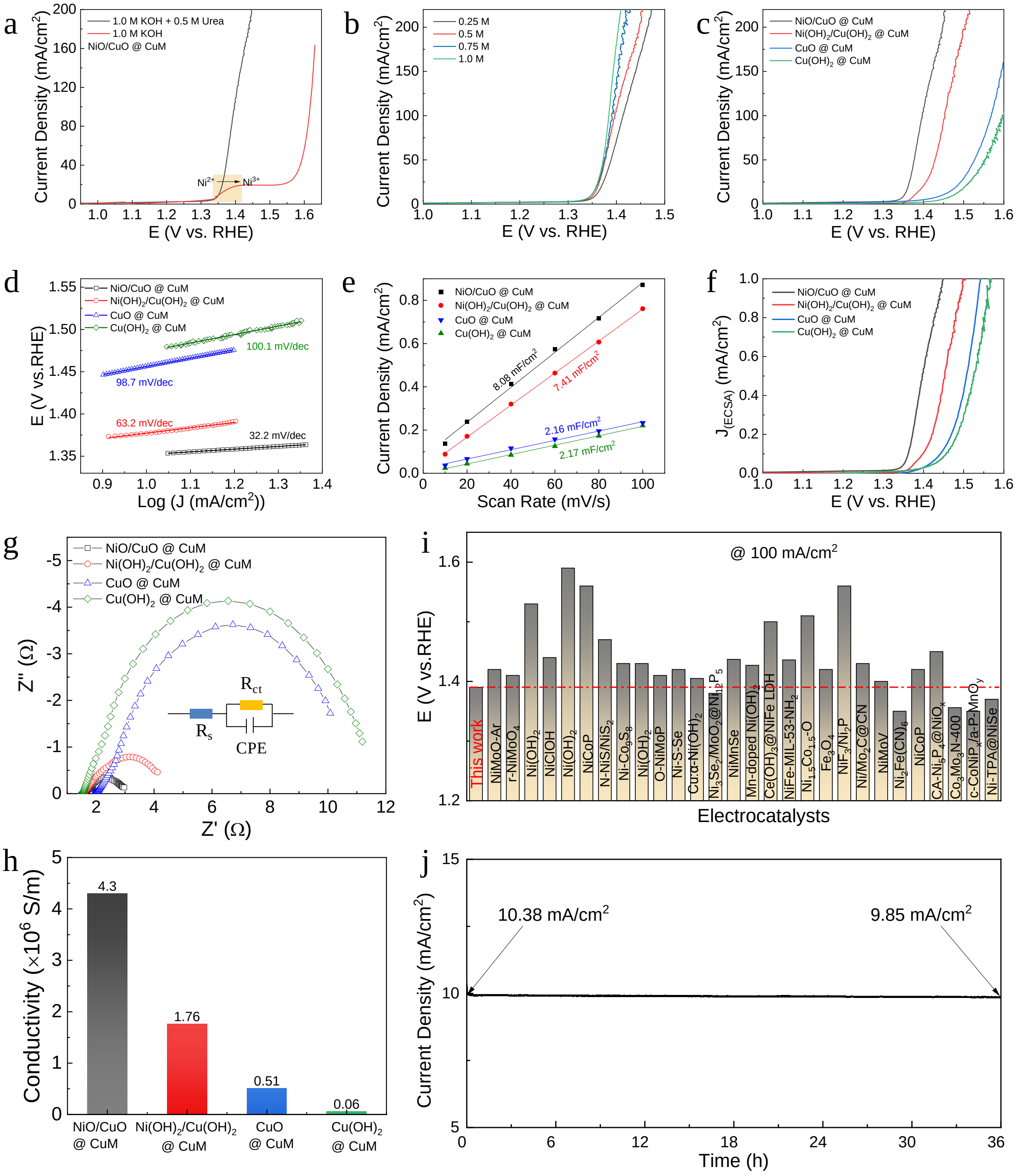

Fig. 3. (a) LSV curves of NiO/CuO@CuM p-p heterojunction electrode in 1.0 M KOH electrolyte with and without 0.5 M urea. (b) LSV curves of NiO/CuO@CuM p-p heterojunction electrode in 1.0 M KOH electrolyte with different concentrations of urea. (c) LSV curves of different self-supported electrodes towards UOR in 1.0 M KOH electrolyte with 0.5 M urea. (d) Tafel slopes, (e) C_{dl} plots obtained from CV curves, (f) LSV curves in 1.0 M KOH electrolyte with 0.5 M urea normalized to ESCA, (g) Nyquist plots

(inset shows the equivalent circuit), and (h) conductivity of the different self-supported electrodes. (i) Comparison of electrochemical UOR performance of this work with other reported electrodes. (j) Stability measurement of NiO/CuO@CuM at the potential of 1.35 V vs. RHE.

Overall, electrochemical results show the formation of the NiOOH to be fundamental for the UOR activation, pointing at Ni^{3+} as the active UOR site. Besides, a comparison with the reference materials and previous reports on NiO/NiOOH/$Ni(OH)_2$ catalysts (**Fig. 3**i and Table S2) also show the CuO@CuM support plays a fundamental role in the process. The support can take a double role. At a local level, at or near the interface between the two materials, CuO can modulate the electronic levels of the NiOOH modifying the adsorption energy of urea and the intermediate and final oxidation products. This effect will be analyzed by DFT calculations in the following section. Besides, at a larger scale, the semiconductor heterostructure can redistribute the charge carrier density, generate an internal electric field, and modify the electronic band structure of the two materials also influencing the adsorption of species in the medium and the transfer of charge carriers.

To gain insight into this latter possible effect, **Figs. 4**a and b show the UPS spectra of NiO/CuO@CuM and CuO@CuM electrodes. Since UPS only probes the surface of the materials, it is reasonable to attribute the measured spectra to the surface of the electrodes, that is NiO and CuO, respectively. The calculated E_{Fermi} are 5.85 eV for NiO and 5.69 eV for CuO relative to the vacuum level. The energy band diagram of the NiO/CuO p-p heterojunction is displayed in **Fig. 4**c. Since the Fermi level of NiO is lower than that of CuO, at the NiO/CuO interface charge is redistributed and an internal built-in electric field is generated. Such p-p heterojunction modulates the surface electronic structure and drives electrons from CuO to NiO at the interface, potentially promoting the adsorption of charge acceptors at the NiO surface.[42] The E_{fb} and N_D can be calculated by fitting the C dependence on the applied voltage through the Mott–Schottky equation.[43] As shown in **Fig. 4**d, the E_{fb} of the NiO/CuO@CuM electrode within a 1.0 M KOH and 0.5 M urea electrolyte is 1.099 V vs. RHE, slightly higher than that of $Ni(OH)_2/Cu(OH)_2$@CuM (0.993 V vs. RHE), CuO@CuM (0.987 V vs. RHE), and $Cu(OH)_2$@CuM (0.976 V vs. RHE) electrodes. The higher E_{fb} value obtained from the NiO/CuO@CuM electrode facilitates charge transfer between the electrolyte and electrode, thus favoring the UOR kinetics. Besides, as shown in **Fig. 4**e, the NiO/CuO@CuM electrode possesses the highest concentration of donors (5.25×10^{20} cm^{-3}), well above that of $Ni(OH)_2/Cu(OH)_2$@CuM (8.52×10^{19} cm^{-3}), CuO@CuM (9.56×10^{19} cm^{-3}) and $Cu(OH)_2$@CuM (2.53×10^{19} cm^{-3}) electrodes, which is consistent with the higher conductivity of the former. Therefore, in the UOR process over the NiO/CuO@CuM catalyst, while the NiOOH derived from the NiO NSs act as the active UOR sites, the CuO NWs play two other roles: i) as support to grow NiO NSs with proper geometry and to transport charge to/from the external circuit; ii) generate a heterojunction with a built-in electric field that promotes electronic transfer at the interface and modulates the surface electrons state, thus promoting the UOR activity of the NiOOH.

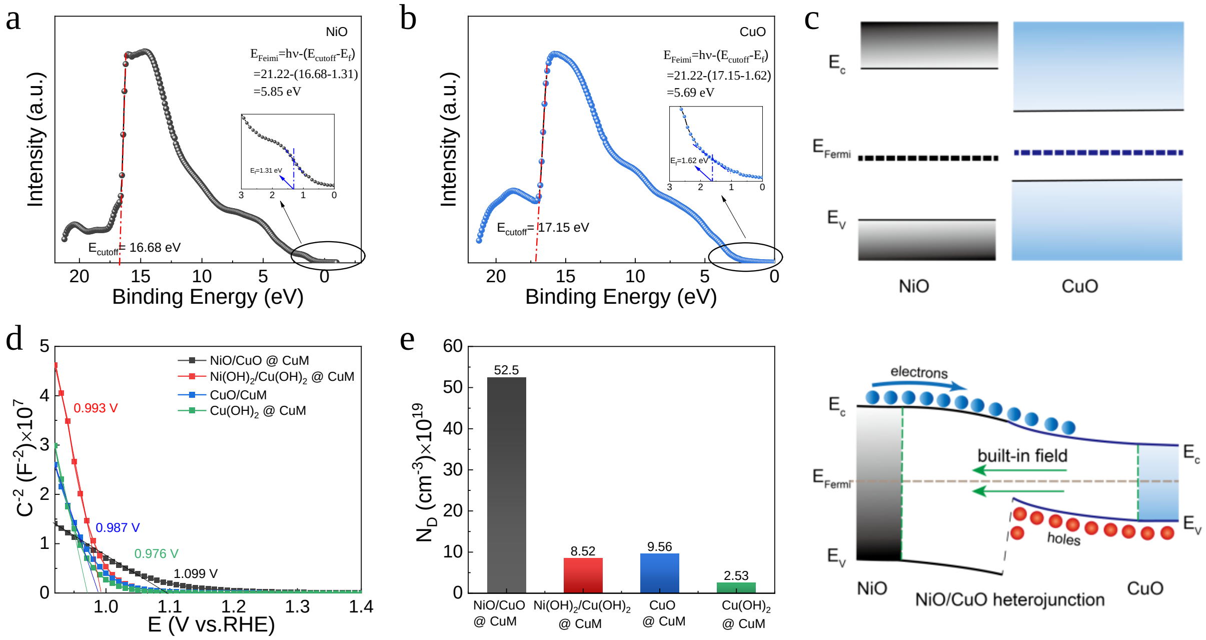

Fig. 4. UPS spectra of (a) NiO/CuO@CuM electrode and (b) CuO@CuM electrode. (c) Schematic diagram of pristine NiO, CuO, and the NiO/CuO p-p heterojunction band structure. (d) Mott-Schottky plots and (e) charge carrier concentration of the different self-supported electrodes in a 1.0 M KOH and 0.5 M urea electrolyte.

3.3. DFT calculation

To gain inside into the effect of the CuO support on the NiOOH electrocatalytic performance at a local level, i.e. at or near the NiOOH/CuO interface, DFT calculations of the very interface between the two materials were carried out. Based on the experimental results, the NiOOH/CuO interphase, and the single crystal structure of NiOOH and CuO were constructed by spin-polarized DFT calculations. The top-view and side-view NiOOH/CuO heterojunction models are shown in Fig. S18. For the lower CuO (101) part, the optimized structure of pure CuO (101) which is similar to the clean CuO (101) was used directly in the NiOOH/CuO model. While for the surface NiOOH part, one layer of β-NiOOH with some OH groups vacancy was chosen to cover the CuO (101). Considering the direct interaction between CuO (101) and β-NiOOH, the OH groups which are close to the CuO (101) were removed. In addition, the structures of optimized NiOOH and CuO (101) are also shown in Fig. S19.

Generally, the urea molecule is primarily adsorbed on the surface of the electrocatalyst during the urea electrooxidation reaction. The adsorption energy of urea on CuO and NiOOH was calculated to be -0.52 and -0.39 eV, which implies that urea is just physically adsorbed on both pristine CuO and pristine NiOOH. In contrast, the adsorption energy of urea on the NiOOH/CuO heterojunction was calculated to be -1.87 eV, which represents a stronger chemical absorption process. This result is consistent with the d-band center calculation as shown in **Fig. 5**a, the d-band center of CuO, NiOOH, and NiOOH/CuO heterojunction were -2.52, -2.46, and -2.14 eV, respectively. According to the d-band center model, the lower the energy level of the d-band center, the weaker binding of the intermediates to the catalyst surface, because more electrons will fill the antibonding states and be occupied when adsorption occurs between the transition metal and adsorbates.[44] **Figs. 5**b-d show the charge density difference of urea adsorbed on pristine CuO, NiOOH, and NiOOH/CuO. There are no chemical bonds and obvious electron transfer either between pristine CuO and the urea molecule or between pristine NiOOH and the urea molecule, while an elongated O-Ni bond can be observed between the Ni atom in the NiOOH/CuO heterojunction and the O atom in the urea molecule. Moreover, **Fig. 5**e and Fig. S20 show the slices of the electron density difference of urea adsorbed on CuO, NiOOH, and NiOOH/CuO. The C-O, C-N, and N-H bond lengths of urea molecules before and after adsorption on NiOOH/CuO are shown in Fig. S21. The C-O bond length of the urea molecule becomes longer, and the C-N bond length becomes shorter due to the formation of an O-Ni bond when the urea molecule is absorbed on NiOOH/CuO. In addition, one of the N-H bond lengths of adsorbed urea on NiOOH/CuO becomes 0.04 Å longer than the free urea molecule, which facilitates the dehydrogenation process. The electrons transfer at the NiOOH/CuO heterojunction is also observed from the slice of electron density difference, as shown in **Fig. 5**e, where the significant electrons accumulate around O atoms in NiOOH and the electrons are depleted around Cu atoms in CuO, implying that electrons transfer from CuO to NiOOH. Besides, DFT calculations show the Cu-O and Ni-O bond lengths at the heterojunction interface to be slightly longer than those in the bulk, as listed in Table S3, which further verifies the interaction of the NiOOH/CuO heterojunction.

In some systems, the CO_2 adsorption energy is a significant parameter determining UOR performance. Thus, the adsorption energy of CO_2 on CuO, NiOOH, and NiOOH/CuO was further comparatively studied. According to DFT calculations, the adsorption energy of CO_2 on CuO, NiOOH, and NiOOH/CuO are -0.01, -0.12, and -0.01 eV, respectively, implying that CO_2 is just very weakly physically adsorbed and thus easily desorbs from the three surfaces. The electron density difference and its corresponding slices of electron density difference of CO_2 adsorbed on CuO, NiOOH, and NiOOH/CuO are shown in **Figs. 5**f-h and Fig. S22. Neither an obvious chemical bond nor electron transfer can be obtained. Moreover, the bonds of adsorbed CO_2 molecules on the CuO, NiOOH, and NiOOH/CuO surfaces keep their original lengths, i.e. that of the free CO_2 molecule, thus facilitating the exposure of the active site for the adsorption of subsequent urea molecule. Thus no significant CO_2 poisoning takes place in these electrocatalysts, which is consistent with the excellent stabilities.

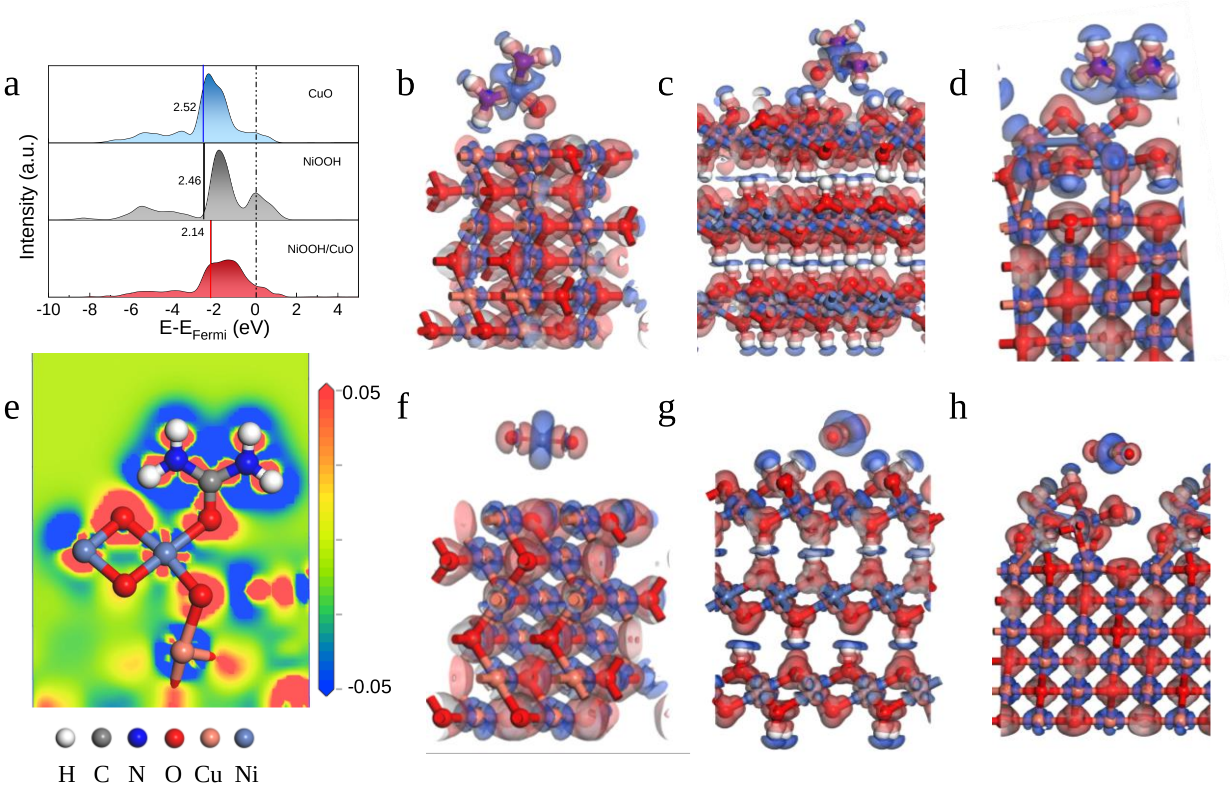

Fig. 5. (a) Partial density of states (PDOS) of pristine CuO, NiOOH, and NiOOH/CuO. The Fermi level is set to zero, and the vertical lines represent the d band center. (b-d) Charge density difference of urea adsorbed on pristine (b) CuO, (c) NiOOH, and (d) NiOOH/CuO. (e) Slices of electron density difference

of urea adsorbed on NiOOH/CuO. The contour around the atoms represents electron accumulation (red) or electron depletion (blue). (f-h) The charge density difference of CO_2 adsorbed on pristine (f) CuO, (g) NiOOH, and (h) NiOOH/CuO. The balls with various colors mean different atoms: red-O, gray-C, white-H, orange-Cu, dark blue-N, and watery blue-Ni.

3.4. Direct urea fuel cells.

DUFCs were assembled using the different self-supported CuM-based electrodes as the anode, 1 M KOH and 0.5 M urea as the anolyte, commercial Pt/C catalyst on carbon paper (CP, Pt/C@CP) as the cathode, and 0.1 M KOH as the catholyte (Fig. S23a). Among the assembled DUFCs, the one based on the NiO/CuO@CuM anode provides the highest OCV at 0.66 V and the maximum power densities at 1.21 mW/cm^2 (Figs. S23b-d). The low dissolved oxygen content in the catholyte hampers the oxygen reduction reaction (ORR) with a theoretical thermodynamic potential of 1.23 V at the cathode, thus limiting the DUFC performance. To reduce the effect of the sluggish cathodic ORR on the DUFCs and more properly compare the different anode materials, 2 M H_2O_2 and 2 M H_2SO_4 were used as the catholyte to take advantage of the much faster kinetics of the H_2O_2 reduction reaction.[45,46] As shown in **Fig. 6**a, in this DUFC configuration, urea is oxidized to N_2 and CO_2 at the anode, and H_2O_2 is reduced to H_2O at the cathode. As expected, the DUFC based on a NiO/CuO@CuM anode exhibits the highest OCV at 0.88 V and a significantly increased current density compared with the DUFCs constructed on other CuM-based anodes (**Figs. 6**b and c). As shown in **Figs. 6**b and d, the NiO/CuO@CuM-based DUFCs exhibit the highest power density of 11.35 mW/cm^2, higher than that of other DUFCS constructed on Ni-based catalysts as the anode reported in recent works (Table S4), demonstrating the high performance of the NiO/CuO@CuM UOR electrocatalyst.

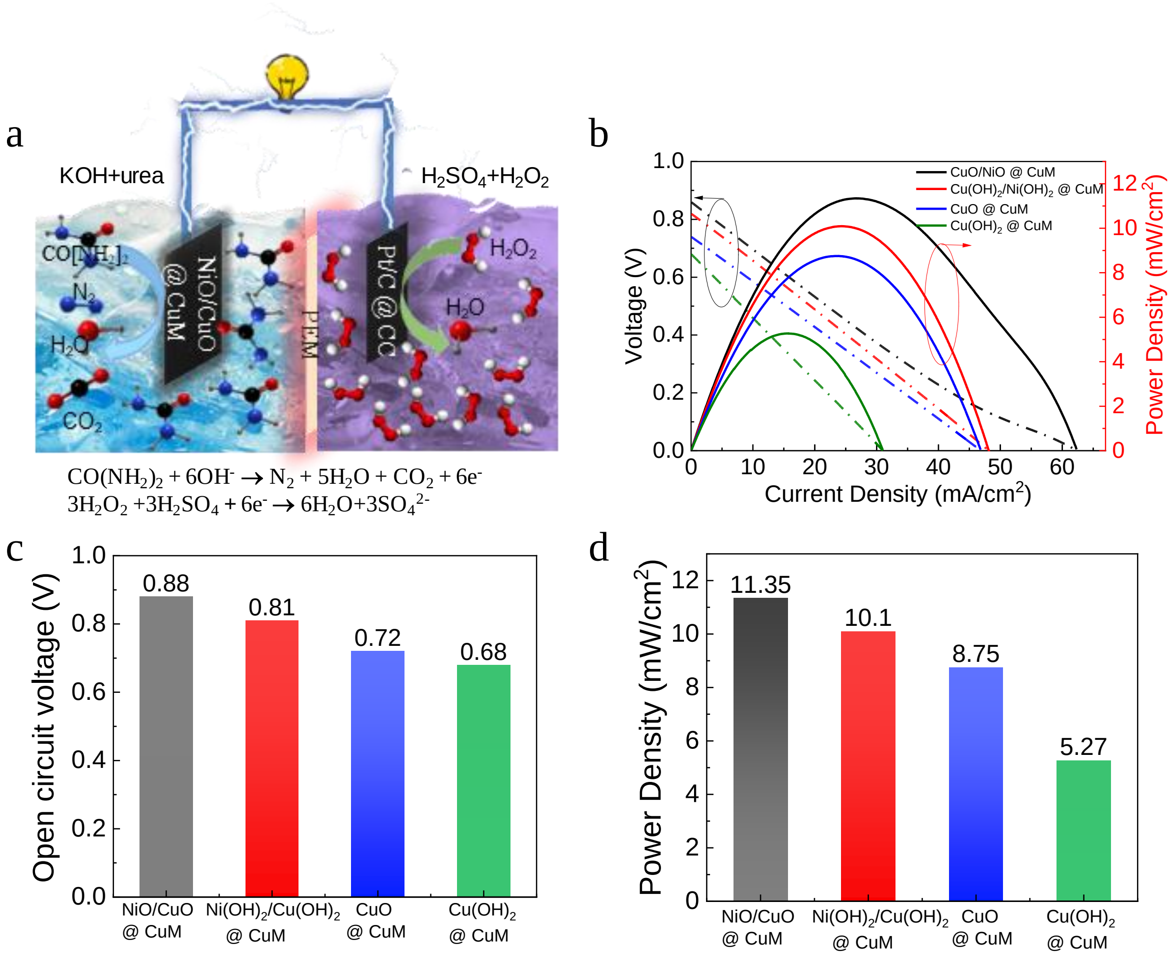

Fig. 6. (a) The structure of DUFCs with a proton exchange membrane (PEM). (b) Voltage-current and power-current curves of DUFCs with different self-supported anodes. (c) Open circuit voltage and (d) power density of DUFCs with different self-supported anodes.

4. Conclusion

Self-supported NiO/CuO@CuM electrodes were produced by combining in-situ etching, chemical deposition, and post-annealing processes, gathering the requirements for industrial large-area electrode production including high throughput, safe, low-cost, and reproducibility. The electrode architecture consists on self–supported p-p heterojunctions formed by NiO NSs vertically grown on CuO NWs which are also vertically grown in this case from the surface of the

CuM. Such NiO/CuO@CuM electrode exhibits excellent UOR performance with a potential of 1.35 V vs. RHE at 10 mA/cm^2 and 1.39 V vs. RHE at 100 mA/cm^2. Using electrochemical and physicochemical characterization tools we demonstrate Ni^{3+} in NiOOH to be the UOR reaction sites. Besides electrochemical characterization and DFT calculations show a double potential effect of the CuO support. Electrochemical characterization shows the energy band level of the NiO/CuO heterojunction and the generated internal built-in electric field modulate the surface electronic states and facilitate electron transfer from CuO to NiO at the interface. The larger flat band potential between the electrolyte and NiO/CuO@CuM electrode verifies the faster charge transportation. Besides, at a very local level, DFT calculations reveal the optimal d band center and electrons transfer from CuO to NiOOH, which benefit the chemical adsorption of urea. Overall, the excellent activity of NiO/CuO@CuM electrode is ascribed to the fast reaction kinetics, low resistance, high conductivity, large active surface area, and the modulated electronic state of NiO/CuO heterojunction. Finally, DUFCs constructed on NiO/CuO@CuM electrode as the anode has an OCV of 0.88 V and an unprecedented power density for this system of 11.35 mW/cm^2.

Supporting Information

Supplementary material related to this article can be found, in the online version.

Declaration of Competing Interest

There are no conflicts to declare.

CRediT authorship contribution statement

LinlinYang: Conceptualization, Methodology, Validation, Investigation, Formal analysis, Data curation, Visualization, Writing–original draft, Writing–review & editing. **Ren He** and **Xiang Wang**: Methodology, Formal analysis, Data curation. **Ting Zhang** and **Jordi Arbiol**: HRTEM, HAADF-STEM EELS characterization, and analysis, Supervision. **Yong Zuo**, **Zhifu Liang**, **Xuan Lu**, and **Junshan Li**: Formal analysis, Visualization. **TingTing Yang** and **Xue Qiang Qi**: DFT calculations and analysis. **Paulina R. Martínez-Alanis** and **Andreu Cabot**: Project administration, Supervision, Funding acquisition, Writing–review & editing.

Acknowledgments

The authors thank the support from the project COMBENERGY, PID2019-105490RB-C32, from the Spanish Ministerio de Ciencia e Innovación. The project on which these results are based has received funding from the European Union's Horizon 2020 research and innovation program under Marie Skłodowska-Curie grant agreement No. 801342 (Tecniospring INDUSTRY) and the Government of Catalonia's Agency for Business Competitiveness (ACCIÓ). ICN2 is supported by the Severo Ochoa program from Spanish MCIN/AEI (Grant No.: CEX2021-001214-S). IREC and ICN2 are funded by the CERCA Programme from the Generalitat de Catalunya. ICN2 acknowledges funding from Generalitat de Catalunya 2017 SGR 327. This study was supported by MCIN with funding from European Union NextGenerationEU (PRTR-C17.I1) and Generalitat de Catalunya. The authors thank the support from the project NANOGEN (PID2020-116093RB-C43), funded by MCIN/ AEI/10.13039/501100011033/ and by "ERDF A way of making Europe", by the "European Union". Part of the present work has been performed in the frameworks of Universitat de Barcelona Nanoscience PhD program. L. L.Yang, X. Wang and X. Lu thank the China Scholarship Council (CSC) for the scholarship support. Z. Liang acknowledges funding from MINECO SO-FPT PhD grant (SEV-2013-0295-17-1). J. Li is grateful for the Natural Science Foundation of Sichuan project (2022NSFSC1229).

References.

[1] K. Dawar, S. Fahad, M.M.R. Jahangir, I. Munir, S.S. Alam, S.A. Khan, I.A. Mian, R. Datta, S. Saud, J. Banout, M. Adnan, M.N. Ahmad, A. Khan, R. Dewil, M. Habib-Ur-Rahman, M.J. Ansari, S. Danish, Biochar and urease inhibitor mitigate NH_3 and N_2O emissions and improve wheat yield in a urea fertilized alkaline soil, Sci. Rep., 11 (2021) 17413.

[2] N. Senthilkumar, G. Gnana kumar, A. Manthiram, 3D hierarchical core-shell nanostructured arrays on carbon fibers as catalysts for direct urea fuel cells, Adv. Energy Mater., 8 (2018) 1702207.

[3] E.T. Sayed, M.A. Abdelkareem, A. Bahaa, T. Eisa, H. Alawadhi, S. Al-Asheh, K.-J. Chae, A.G. Olabi, Synthesis and performance evaluation of various metal chalcogenides as active anodes for direct urea fuel cells, Renew. Sust. Energ. Rev., 150 (2021) 111470.

[4] Y. Xu, T. Ren, K. Ren, S. Yu, M. Liu, Z. Wang, X. Li, L. Wang, H. Wang, Metal-organic frameworks-derived Ru-doped Co_2P/N-doped carbon composite nanosheet arrays as bifunctional electrocatalysts for hydrogen evolution and urea oxidation, Chem. Eng. J., 408 (2021) 127308.

[5] B. Zhu, Z. Liang, R. Zou, Designing advanced catalysts for energy conversion based on urea oxidation reaction, Small, 16 (2020) e1906133.

[6] F. Guo, K. Ye, M. Du, X. Huang, K. Cheng, G. Wang, D. Cao, Electrochemical impedance analysis of urea electro-oxidation mechanism on nickel catalyst in alkaline medium, Electrochim. Acta, 210 (2016) 474-482.

[7] C. Xiao, S. Li, X. Zhang, D.R. MacFarlane, MnO_2/$MnCo_2O_4$/Ni heterostructure with quadruple hierarchy: a bifunctional electrode architecture for overall urea oxidation, J. Mater. Chem. A, 5 (2017) 7825-7832.

[8] J. Li, S. Wang, J. Chang, L. Feng, A review of Ni based powder catalyst for urea oxidation in assisting water splitting reaction, Adv. Powder. Mater., (2022) 100030.

[9] G. Wang, J. Chen, Y. Li, J. Jia, P. Cai, Z. Wen, Energy-efficient electrolytic hydrogen production assisted by coupling urea oxidation with a pH-gradient concentration cell, Chem. Commun., 54 (2018) 2603-2606.

[10] S. Nangan, Y. Ding, A. Z. Alhakemy, Y. Liu, Z. Wen, Hybrid alkali-acid urea-nitrate fuel cell for degrading nitrogen-rich wastewater, Appl. Catal. B-Environ., 286 (2021).

[11] Y. Wang, C. Wang, H. Shang, M. Yuan, Z. Wu, J. Li, Y. Du, Self-driven Ru-modified NiFe MOF nanosheet as multifunctional electrocatalyst for boosting water and urea electrolysis, J. Colloid Interface Sci., 605 (2022) 779-789.

[12] H. Sun, J. Liu, G. Chen, H. Kim, S. Kim, Z. Hu, J.M. Chen, S.C. Haw, F. Ciucci, W. Jung, Hierarchical structure of CuO nanowires decorated with $Ni(OH)_2$ supported on Cu foam for hydrogen production via urea electrocatalysis, Small Methods, 6 (2022) e2101017.

[13] Z.-Y. Yu, C.-C. Lang, M.-R. Gao, Y. Chen, Q.-Q. Fu, Y. Duan, S.-H. Yu, Ni–Mo–O nanorod-derived composite catalysts for efficient alkaline water-to-hydrogen conversion via urea electrolysis, Energy Environ. Sci., 11 (2018) 1890-1897.

[14] J. Zhang, T. Quast, W. He, S. Dieckhofer, J.R.C. Junqueira, D. Ohl, P. Wilde, D. Jambrec, Y.T. Chen, W. Schuhmann, In situ carbon corrosion and Cu leaching as a strategy for boosting oxygen evolution reaction in multimetal electrocatalysts, Adv. Mater., (2022) e2109108.

[15] Y. Wang, X. Li, M. Zhang, J. Zhang, Z. Chen, X. Zheng, Z. Tian, N. Zhao, X. Han, K. Zaghib, Y. Wang, Y. Deng, W. Hu, Highly active and durable single-atom tungsten-doped $NiS_{0.5}$ $Se_{0.5}$ Nanosheet @ $NiS_{0.5}$ $Se_{0.5}$ nanorod heterostructures for water splitting, Adv. Mater., (2022) e2107053.

[16] S. H. Han, H.M. Liu, P. Chen, J.X. Jiang, Y. Chen, Porous trimetallic PtRhCu cubic nanoboxes for ethanol electrooxidation, Adv. Energy Mater., 8 (2018) 1801326.

[17] P. F. Yin, M. Zhou, J. Chen, C. Tan, G. Liu, Q. Ma, Q. Yun, X. Zhang, H. Cheng, Q. Lu, B. Chen, Y. Chen, Z. Zhang, J. Huang, D. Hu, J. Wang, Q. Liu, Z. Luo, Z. Liu, Y. Ge, X.J. Wu, X.W. Du, H. Zhang, Synthesis of palladium-based crystalline@amorphous core-shell nanoplates for highly efficient ethanol oxidation, Adv. Mater., 32 (2020) e2000482.

[18] J. Wang, T. Fu, F. Meng, D. Zhao, S.S.C. Chuang, Z. Li, Highly active catalysis of methanol oxidative carbonylation over nano Cu_2O supported on micropore-rich mesoporous carbon, Appl. Catal. B-Environ., 303 (2022) 120890.

[19] H. Ma, Z. Zheng, H. Zhao, C. Shen, H. Chen, H. Li, Z. Cao, Q. Kuang, H. Lin, Z. Xie, Trimetallic PtNiCo branched nanocages as efficient and durable bifunctional electrocatalysts towards oxygen reduction and methanol oxidation reactions, J. Mater. Chem. A, 9 (2021) 23444-23450.

[20] Y. Guo, J. Liu, Y.-T. Xu, B. Zhao, X. Wang, X.-Z. Fu, R. Sun, C.-P. Wong, In situ redox growth of mesoporous Pd-Cu_2O nanoheterostructures for improved glucose oxidation electrocatalysis, Sci. Bull., 64 (2019) 764-773.

[21] W. J. Liu, Z. Xu, D. Zhao, X.Q. Pan, H.C. Li, X. Hu, Z.Y. Fan, W.K. Wang, G.H. Zhao, S. Jin, G.W. Huber, H.Q. Yu, Efficient electrochemical production of glucaric acid and H_2 via glucose electrolysis, Nat. Commun., 11 (2020) 265.

[22] J. Li, S. Wang, J. Chang, L. Feng, A review of Ni based powder catalyst for urea oxidation in assisting water splitting reaction, Advanced Powder Materials, (2022) 100030.

[23] L. Zhang, L. Wang, H. Lin, Y. Liu, J. Ye, Y. Wen, A. Chen, L. Wang, F. Ni, Z. Zhou, S. Sun, Y. Li, B. Zhang, H. Peng, A lattice-oxygen-involved reaction pathway to boost urea oxidation, Angew Chem. Int. Ed., 58 (2019) 16820-16825.

[24] Z. Ji, Y. Song, S. Zhao, Y. Li, J. Liu, W. Hu, Pathway manipulation via Ni, Co, and V ternary synergism to realize high efficiency for urea electrocatalytic oxidation, ACS Catal., 12 (2021) 569-579.

[25] S.-K. Geng, Y. Zheng, S.-Q. Li, H. Su, X. Zhao, J. Hu, H.-B. Shu, M. Jaroniec, P. Chen, Q.-H. Liu, S.-Z. Qiao, Nickel ferrocyanide as a high-performance urea oxidation electrocatalyst, Nat. Energy, 6 (2021) 904-912.

[26] X. Xu, J. Li, C. Zhang, S. Zhang, G. Su, Z. Shi, H. Wang, M. Huang, Controllable transition engineering from homogeneous $NiSe_2$ nanowrinkles to heterogeneous $Ni_3Se_4/NiSe_2$ rod-like nanoarrays for promoted urea-rich water oxidation at large current densities, Applied Catalysis B: Environmental, 319 (2022) 121949.

[27] X. Xu, Q. Deng, H.C. Chen, M. Humayun, D. Duan, X. Zhang, H. Sun, X. Ao, X. Xue, A. Nikiforov, K. Huo, C. Wang, Y. Xiong, Metal-organic frameworks offering tunable binary active sites toward highly efficient urea oxidation electrolysis, Research, 2022 (2022) 9837109.

[28] Y. Zeng, Z. Cao, J. Liao, H. Liang, B. Wei, X. Xu, H. Xu, J. Zheng, W. Zhu, L. Cavallo, Z. Wang, Construction of hydroxide pn junction for water splitting electrocatalysis, Appl. Catal. B-Environ., 292 (2021) 120160.

[29] V. R. Stamenkovic, D. Strmcnik, P.P. Lopes, N.M. Markovic, Energy and fuels from electrochemical interfaces, Nature Mater., 16 (2016) 57-69.

[30] S. Ni, H. Qu, Z. Xu, X. Zhu, H. Xing, L. Wang, J. Yu, H. Liu, C. Chen, L. Yang, Interfacial engineering of the $NiSe_2/FeSe_2$ p-p heterojunction for promoting oxygen evolution reaction and electrocatalytic urea oxidation, Appl. Catal. B-Environ., 299 (2021) 120638.

[31] C. C. McCrory, S. Jung, J. C. Peters, T.F. Jaramillo, Benchmarking heterogeneous electrocatalysts for the oxygen evolution reaction, J. Am. Chem. Soc., 135 (2013) 16977-16987.

[32] G. Shao, Work Function and Electron Affinity of Semiconductors: Doping effect and complication due to fermi level pnning, Energy & Environ. Mater., 4 (2021) 273-276.

[33] L. Yang, J. Chen, K. Ge, J. Guo, Q. Duan, F. Li, Y. Xu, Y. Mai, Polymer/Si heterojunction hybrid solar cells with Rubrene:DMSO organic semiconductor film as an electron-selective contact, J. Phys. Chem. C, 122 (2018) 23371-23376.

[34] K. Ge, J. Chen, B. Chen, Y. Shen, J. Guo, F. Li, H. Liu, Y. Xu, Y. Mai, Low work function intermetallic thin film as a back surface field material for hybrid solar cells, Sol. Energy, 162 (2018) 397-402.

[35] L. Zhuang, L. Ge, Y. Yang, M. Li, Y. Jia, X. Yao, Z. Zhu, Ultrathin iron-cobalt oxide nanosheets with abundant oxygen vacancies for the oxygen evolution reaction, Adv. Mater., 29 (2017), 1606793.

[36] Y. Zhou, C.-K. Dong, L.L. Han, J. Yang, X.-W. Du, Top-down preparation of active cobalt oxide catalyst, ACS Catal., 6 (2016), 6699-6703.

[37] J. Chastain, RC King Jr. Handbook of X-ray photoelectron spectroscopy, Perkin-Elmer Corporation 40 (1992), 221.

[38] B. R. Reddy, G. S. Harish, C. S. Reddy, P. S. Reddy, Synthesis and characterization of Cu doped NiO nanoparticles. Int. J. Mod. Eng. Res, 4(6), (2014), 62-66.

[39] S. Deabate, F. Fourgeot, F. Henn, X-ray diffraction and micro-Raman spectroscopy analysis of new nickel hydroxide obtained by electrodialysis. J. Power Sources 87, (2000), 125–136.

[40] Z. Shi, Z. Yu, J. Guo, R. Jiang, Y. Hou, Y. Chen, H. Chen, M. Wang, H. Pang, W. Tang, Lattice distortion of crystalline-amorphous nickel molybdenum sulfide nanosheets for high-efficiency overall water splitting: libraries of lone pairs of electrons and in situ surface reconstitution, Nanoscale, 14 (2022) 1370-1379.

[41] C. Sudakar, J. S. Thakur, G. Lawes, R. Naik, V. M. Naik, Ferromagnetism induced by planar nanoscale CuO inclusions in Cu-doped ZnO thin films, Phys. Rev. B, 75 (2007).

[42] M. Yuan, J. Chen, Y. Bai, Z. Liu, J. Zhang, T. Zhao, Q. Shi, S. Li, X. Wang, G. Zhang, Electrochemical C-N coupling with perovskite hybrids toward efficient urea synthesis, Chem. Sci., 12 (2021) 6048-6058.

[43] F. Cardon, W. P Gomes, On the determination of the flat-band potential of a semiconductor in contact with a metal or an electrolyte from the Mott-Schottky plot, J. Phys. D: Appl. Phys. 11 (1978) L63-L67.

[44] J.K. Norskov, T. Bligaard, J. Rossmeisl, C.H. Christensen, Towards the computational design of solid catalysts, Nature Chem., 1 (2009) 37-46.

[45] G.H. Miley, N. Luo, J. Mather, R. Burton, G. Hawkins, L. Gu, E. Byrd, R. Gimlin, P.J. Shrestha, G. Benavides, J. Laystrom, D. Carroll, Direct $NaBH_4/H_2O_2$ fuel cells, J. Power Sources, 165 (2007) 509-516.

[46] S.J. Lao, H.Y. Qin, L.Q. Ye, B.H. Liu, Z.P. Li, A development of direct hydrazine/hydrogen peroxide fuel cell, J. Power Sources, 195 (2010) 4135-4138.

Supporting Information

Click here to access/download

Supporting Information

linlinyang et al_SI.pdf

Declaration of interests

☒The authors declare that they have no known competing financial interests or personal relationships that could have appeared to influence the work reported in this paper.

☐The authors declare the following financial interests/personal relationships which may be considered as potential competing interests:

LinlinYang: Conceptualization, Methodology, Validation, Investigation, Formal analysis, Data curation, Visualization, Writing–original draft, Writing–review & editing. **Ren He** and **Xiang Wang**: Methodology, Formal analysis, Data curation. **Ting Zhang** and **Jordi Arbiol**: HRTEM, HAADF-STEM EELS characterization, and analysis, Supervision. **Yong Zuo**, **Zhifu Liang**, **Xuan Lu**, and **Junshan Li**: Formal analysis, Visualization. **TingTing Yang** and **Xue Qiang Qi**: DFT calculations and analysis. **Paulina R. Martínez-Alanis** and **Andreu Cabot**: Project administration, Supervision, Funding acquisition, Writing–review & editing.

Graphical Abstract